

# PID: Physics-Informed Diffusion Model for Infrared Image Generation

Fangyuan Mao<sup>a,b</sup>, Jilin Mei<sup>a</sup>, Shun Lu<sup>a,b</sup>, Fuyang Liu<sup>a,b</sup>, Liang Chen<sup>a</sup>, Fangzhou Zhao<sup>a</sup>, Yu Hu<sup>a,b</sup>

<sup>a</sup>*Institute of Computing Technology, Chinese Academy of Sciences, Beijing, 100190, China*

<sup>b</sup>*University of Chinese Academy of Sciences, Beijing, 101408, China*

---

## Abstract

Infrared imaging technology has gained significant attention for its reliable sensing ability in low visibility conditions, prompting many studies to convert the abundant RGB images to infrared images. However, most existing image translation methods treat infrared images as a stylistic variation, neglecting the underlying physical laws, which limits their practical application. To address these issues, we propose a **Physics-Informed Diffusion (PID)** model for translating RGB images to infrared images that adhere to physical laws. Our method leverages the iterative optimization of the diffusion model and incorporates strong physical constraints based on prior knowledge of infrared laws during training. This approach enhances the similarity between translated infrared images and the real infrared domain without increasing extra training parameters. Experimental results demonstrate that PID significantly outperforms existing state-of-the-art methods. Our code is available at <https://github.com/fangyuanmao/PID>.

*Keywords:* Physical constraints, Diffusion model, Infrared image generation

---

## 1. Introduction

Infrared images offer strong anti-interference capabilities and demonstrates resilience in complex weather conditions like night, rain, dust, and snow. In fields like robotics and autonomous driving, there is a growing demand of infrared images fusion for perception tasks [1]. However, acquiring infrared images requires specialized devices, which makes the availability of open-source infrared datasets significantly lag behind that of RGB image datasets. Many previous studies have tried to translate RGB images to infrared images to augment infrared datasets [2, 3, 4].

Existing methods have utilized Variational Autoencoders (VAEs [5]) or Generative Adversarial Networks (GANs [6]) to translate RGB images to infrared images. Although VAEs are well-suited for image translation, the resulting images often lack sharpness [7], which makes it challenging for downstream tasks to extract effective infrared features. GANs have also become a popular approach for generating infrared images. However, GAN-based methods suffer from training instabilities and mode collapse problems [8].

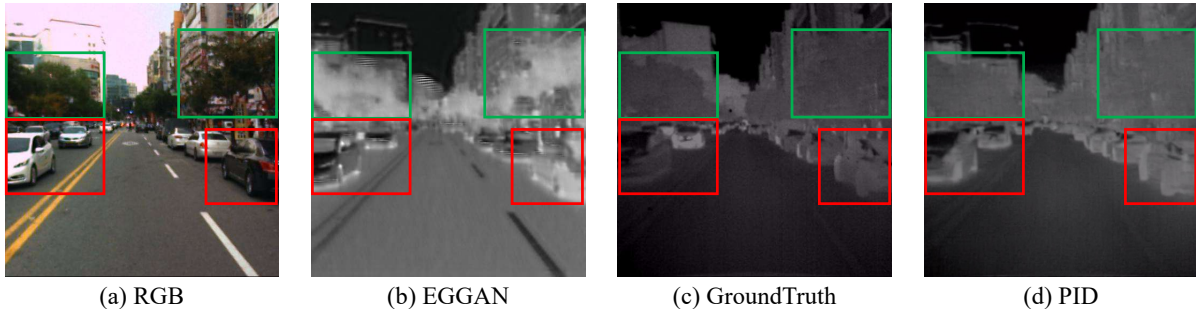


Fig. 1: Translated infrared image based on RGB image via different methods. The image generated by EGGAN [4] shows physical inaccuracies, such as trees appearing significantly hotter than cars (lighter grey color represents higher temperature). Our result is closer to the GroundTruth and adds details in accordance with physical laws, such as the heat generated by moving tires.

Over the last few years, Diffusion Models [9, 10] (DMs) have gained tremendous progress in image synthesis [11, 8] and related domains [12]. DMs enable us to model the rich distribution of the target image domain through iterative sampling. Notably, DMs do not encounter training instabilities as in GANs and have exhibited exceptional generation quality. These achievements have motivated our exploration of a diffusion-based method for infrared image generation.

Meanwhile, the aforementioned generative works neglect the underlying physical laws. While the generated images may retain edge information, they may significantly differ from the actual physical characteristics of infrared scenes (e.g., a moving cold car under a hot tree generated by EGGAN in Fig. 1). Such deviations from real-world physical laws may cause accumulated biases in downstream tasks, leading to incorrect recognition of infrared features. Given the effectiveness of physical laws in modeling these infrared images, it is natural to incorporate them into generative models.

In this paper, we present PID, a **Physics-Informed Diffusion** model for infrared image generation that translates RGB images into infrared images. The effectiveness of PID is illustrated in Fig. 1. By harnessing the iterative optimization of diffusion models and conducting sampling in the latent space, latent diffusion models [10] (LDMs) offer a powerful solution for efficiently generating high-quality infrared images.

To impose physical constraints on the translated images, we utilize the physical laws that govern the components of infrared imaging. The TeX method [13] decomposes infrared images into fundamental physical components (Temperature ( $T$ ), Emissivity ( $e$ ), and Thermal texture ( $X$ )). While it effectively analyzes images in physical space, its practical application is hindered by the requirement for multiple infrared spectra and filters. Considering that publicly available datasets mainly consist of superimposed spectra infrared images directly captured by infrared cameras [14], we propose a TeV decomposition method designed for general superimposed spectra infrared images. By applying the TeV decomposition with self-supervised training, we develop TeVNet ( $\mathcal{N}_{\text{TeV}}$ ) to effectively decompose the infrared images. During the training of LDMs, we incorporate two physical losses,  $\mathcal{L}_{\text{Rec}}$  and  $\mathcal{L}_{\text{TeV}}$ ,

based on the decomposed information from  $\mathcal{N}_{\text{TeV}}$ , ensuring adherence to physical laws at every diffusion model sampling step.

Our PID method leverages prior knowledge of physical laws and infrared images, to incorporate physical constraints during the training of the latent diffusion model, thereby enhancing the fidelity of translated infrared images to the target infrared domain without increasing extra training parameters. In summary, our contributions are as follows:

- By analyzing the intrinsic characteristics of infrared image translation, we discover a more suitable approach by adopting LDMs to translate RGB images into infrared images of superior quality.
- Through the integration of physical constraints, our method guarantees the adherence of the translated images to fundamental physical laws, facilitating the application in downstream tasks.
- We propose an efficient TeV decomposition method for general superimposed spectra infrared images directly captured by infrared camera, simplifying data collection, and broadening its applicability.
- Our proposed method achieves state-of-the-art (**SOTA**) results on multiple metrics in FLIR and KAIST datasets. Compared to the latest RGB-to-infrared translation method [4], the FID scores decreased by 45.14 and 55.75 on the KAIST and FLIR datasets, respectively.

## 2. Related work

Regarding infrared images generation, there are two main approaches: simulator-based generation and image translation based on RGB images. The infrared images generated by simulators often show isotropy and excessive smoothness [15], which is far from real infrared images. Consequently, numerous studies [2, 3, 4] have focused on the image translation method. In the following section, we will focus on generative models for infrared images translation.

### 2.1. Generative model for infrared images translation

VAEs [5] learn to encode source RGB images into latent vectors and decode target domain images from sampled latent vectors. However, the simplistic posterior distribution of VAEs leads to sub-optimal generation results. GANs [6], by establishing the generation process as an adversarial game, enhance the quality of image translation. Conditional GANs (CGANs [16]) use CNNs to learn the mapping from a conditional input image to an output image. Pix2Pix [17], based on CGAN, integrates the GAN objective with L1 loss to ensure that the translated images closely resemble the ground truth. CycleGAN [18] incorporates cycle consistency loss for image domain transfer tasks and is capable of training unpaired images. However, [19] points out that unsupervised CycleGAN is susceptible to unpredictable content during the translation process. Many works based on GANs [20, 21, 22, 23, 24]

improve network architectures and introduce stronger constraint loss functions to enhance model performance. For example, Edge-guided GAN [4] emphasizes edge consistency across different image domains. Nonetheless, GANs often encounter difficulties in training and produce translated images of unsatisfactory quality.

*Our method is based on the latent diffusion model, which can be efficiently trained to convergence and is capable of translating detailed and realistic high-quality infrared images from RGB images.*

## 2.2. Diffusion model for image translation

Diffusion models [9, 25, 26, 27] have attracted considerable attention for image generation. Diffusion models employ a series of steps to model the diffusion process between Gaussian noise and image domain distribution. These methods train diffusion models (typically UNet) to predict Gaussian noise added at different time steps. By step-by-step denoising, the diffusion model can obtain clean, high-quality translated images, leading to remarkable progress in various image processing fields, including image generation [28], image restoration [29], and image translation [8]. To improve computational efficiency, the Latent diffusion model (LDM [10]) encodes images into latent space vectors, performs the diffusion and denoising process in the latent space, and then decodes the latent vectors into pixel space to generate images. LDM converts high-dimensional pixel space generation to low-dimensional latent space generation.

Despite much progress in diffusion models for RGB image generation, there is a gap in infrared image generation. The target infrared image domain differs significantly from the RGB image domain, making existing pre-trained RGB generation models ineffective. Moreover, previous works have treated infrared images merely as a style, without considering the physical laws governing infrared images.

*Our method fully leverages prior knowledge of infrared images to incorporate strong physical constraints during the training of LDMs. As far as we know, we are the first to incorporate physical loss into infrared images generative models. Our method enhances the similarity between translated images and the target domain without increasing extra training parameters.*

## 3. Methodology

### 3.1. Preliminary

#### 3.1.1. Diffusion model

Given an input ground truth image  $\mathbf{x}_0 \sim p_{data}$ , we define a series of noisy images  $q(\mathbf{x}_{1:T}|\mathbf{x}_0) = \prod_{t=1}^T q(\mathbf{x}_t|\mathbf{x}_{t-1})$  by incrementally adding Gaussian noise, modeled as a Markov chain,

$$\mathbf{x}_t = \sqrt{\alpha_t}\mathbf{x}_{t-1} + \sqrt{1 - \alpha_t}\boldsymbol{\epsilon}, \quad (1)$$

$$q(\mathbf{x}_t|\mathbf{x}_{t-1}) = \mathcal{N}(\mathbf{x}_t|\sqrt{\alpha_t}\mathbf{x}_{t-1}, (1 - \alpha_t)\mathbf{I}), \quad (2)$$

where  $\boldsymbol{\epsilon} \sim \mathcal{N}(\mathbf{0}, \mathbf{I})$ ,  $\alpha_i \in (0, 1)$ . We can characterize the distribution of  $\mathbf{x}_t$  given  $\mathbf{x}_0$  by simplifying intermediate steps as

$$\mathbf{x}_t = \sqrt{\bar{\alpha}_t} \mathbf{x}_0 + \sqrt{1 - \bar{\alpha}_t} \boldsymbol{\epsilon}, \quad (3)$$

$$q(\mathbf{x}_t | \mathbf{x}_0) = \mathcal{N}(\mathbf{x}_t | \sqrt{\bar{\alpha}_t} \mathbf{x}_0, (1 - \bar{\alpha}_t) \mathbf{I}), \quad (4)$$

where  $\bar{\alpha}_t = \prod_{i=1}^t \alpha_i$ . The reverse process also forms a Markov chain starting with pure Gaussian noise,  $\mathbf{x}_T \sim \mathcal{N}(\mathbf{0}, \mathbf{I})$ . Through reverse iterative sampling, a high-quality image without noise is ultimately obtained.

$$p_\theta(\mathbf{x}_{0:T}) = p(\mathbf{x}_T) \prod_{t=1}^T p_\theta(\mathbf{x}_{t-1} | \mathbf{x}_t). \quad (5)$$

$$p_\theta(\mathbf{x}_{t-1} | \mathbf{x}_t) = \mathcal{N}(\boldsymbol{\mu}_\theta(\mathbf{x}_t; t, \mathbf{c}), \sigma_t^2 \mathbf{I}). \quad (6)$$

By introducing the condition  $\mathbf{c}$ , we establish the conditional diffusion model. In image translation tasks,  $\mathbf{c}$  represents an image condition (e.g., the low-resolution input in super-resolution tasks [11] or the RGB image in our translation task). The essence of the diffusion model lies in training a denoising model  $\boldsymbol{\epsilon}_\theta$ :

$$\theta^* = \arg \min_{\theta} \mathbb{E}_{\mathbf{x} \sim p_{data}, \boldsymbol{\epsilon} \sim \mathcal{N}(\mathbf{0}, \mathbf{I})} [\mathcal{L}_{\text{Noise}}(\boldsymbol{\epsilon}, \boldsymbol{\epsilon}_\theta(\mathbf{x}_t; t, \mathbf{c}))]. \quad (7)$$

The output noise of  $\boldsymbol{\epsilon}_\theta$  is utilized to obtain  $\boldsymbol{\mu}_\theta$ .  $\mathcal{L}_{\text{Noise}}$  is defined as the L1 loss to quantify the discrepancy between the predicted noise  $\boldsymbol{\epsilon}_\theta$  and the actual added noise  $\boldsymbol{\epsilon}$ . Please refer to Appendix A for complete derivation.

### 3.1.2. Latent diffusion model

LDM [10] first encodes target domain images into latent space vectors using a VAE encoder, represented as  $\mathbf{z} = \mathcal{E}(\mathbf{x})$ . Noised vectors  $\mathbf{z}_t = \sqrt{\bar{\alpha}_t} \mathbf{z}_0 + \sqrt{1 - \bar{\alpha}_t} \boldsymbol{\epsilon}$  are then used to train the denoising model in the latent space. During inference, the VAE decoder generates images in the target domain from latent space vectors sampled by diffusion model, represented as  $\hat{\mathbf{x}}_0 = \mathcal{D}(\hat{\mathbf{z}}_0)$ . By compressing the sampling space, LDM significantly enhances generation efficiency.

### 3.2. TeV decomposition

[30] decomposes infrared images into temperature  $T$  and emissivity  $e$  for remote sensing images using an iterative approach. More recently, [13] uses a network to obtain  $T$ ,  $e$ , and thermal texture  $X$ . Inspired by these works, we propose decomposing components of the translated infrared images to ensure compliance with physical laws.

Firstly, it is crucial to understand the source of infrared thermal radiation. In thermodynamics, a black body is an idealized object that absorbs all incoming electromagnetic radiation. The thermal radiation emitted by a black body depends solely on its temperature. The emissivity of a black body is defined as  $e = 1$ . The relationship between radiation power and temperature is described by Planck’s black body equation [31]. In reality, an ideal black body does not exist; therefore, a gray body [32] is used to approximate real-world objects.

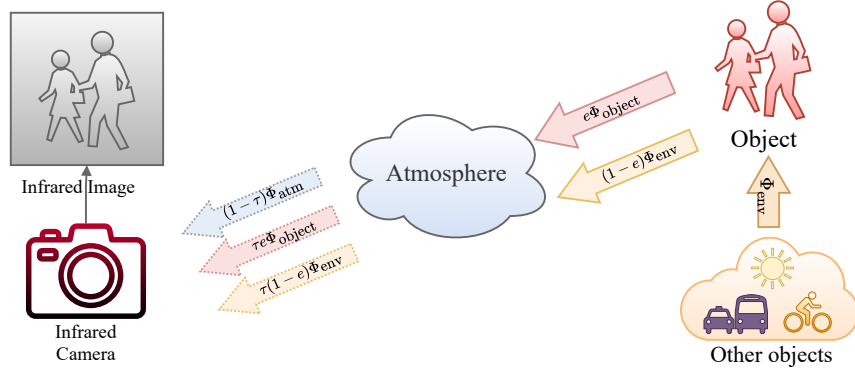


Fig. 2: The infrared signal transmission chain when an infrared camera captures an image of pedestrians. The captured infrared signal primarily includes three components: thermal radiation emitted by the object  $\Phi_{\text{object}}$ , thermal radiation reflected from other objects  $\Phi_{\text{env}}$ , and atmospheric thermal radiation  $\Phi_{\text{atm}}$ .  $\tau$  represents transmissivity of atmosphere while  $e$  represents emissivity of detected object.

A gray body's emissivity is defined as  $0 < e < 1$ , indicating that it reflects a portion of the radiation energy.

As illustrated in Fig. 2, a typical infrared image at wavelength  $\lambda$  collected by an infrared camera can be described as a superposition of the thermal radiation emitted by the object itself, the reflection of radiation from other objects, and atmospheric radiation.

$$S_{\lambda} = \tau_{\text{atm}} e_{\lambda} \Phi_{\text{object}}(T) + \tau_{\text{atm}} (1 - e_{\lambda}) \Phi_{\text{env}}(T) + (1 - \tau_{\text{atm}}) \Phi_{\text{atm}}(T), \quad (8)$$

where  $S_{\lambda}$  represents the infrared signal at wavelength  $\lambda$ . The first term can be expressed as

$$\tau_{\text{atm}} e_{\lambda} \Phi_{\text{object}}(T) = \tau_{\text{atm}} e_{\lambda} B_{\lambda}(T), \quad (9)$$

where  $\tau_{\text{atm}}$  represents the transmissivity of atmosphere [33], and  $e_{\lambda}$  denotes the object's emissivity at wavelength  $\lambda$ .  $e_{\lambda}$  is only related to the material of object. The infrared thermal radiation intensity of a black body  $\Phi_{\text{object}}$  is determined by Planck's law [31] with  $B_{\lambda}(T)$ . Planck's law is given by:

$$\Phi_{\text{object}}(T) = B_{\lambda}(T) = \frac{2\pi h c^2}{\lambda^5} \frac{1}{e^{\frac{hc}{\lambda k T}} - 1}, \quad (10)$$

where  $h$  is Planck constant,  $k$  is Boltzmann constant, and  $c$  is the speed of light.  $\lambda$  is the detected wavelength and  $T$  is the temperature of black body. Therefore, the infrared thermal radiation intensity of a black body is solely determined by the wavelength and temperature.

The reflection of radiation from other objects and atmospheric radiation can be summarized as,

$$\tau_{\text{atm}} (1 - e_{\lambda}) \Phi_{\text{env}}(T) + (1 - \tau_{\text{atm}}) \Phi_{\text{atm}}(T), \quad (11)$$

where  $\Phi_{\text{env}}$  and  $\Phi_{\text{atm}}$  denote the radiation from other objects and atmosphere, respectively.

Due to the absorption of infrared radiation by water vapor and carbon dioxide in the atmosphere, observed infrared images typically have  $\tau_{\text{atm}} \approx 1$ , leading to the approximation of  $S_\lambda$

$$S_\lambda \approx e_\lambda B_\lambda(T) + (1 - e_\lambda) \Phi_{\text{env}}(T). \quad (12)$$

TeX [13] proposes that  $\Phi_{\text{env}}$  at pixel coordinates  $\alpha = (x, y)$  originates from a linear combination of the infrared signal values of its  $N-1$  neighboring pixels  $\beta = \{(x_1, y_1), \dots, (x_{N-1}, y_{N-1})\}$ , where  $H \times W$  refers to the image size and  $N = H \times W$  denotes the total number of pixels.

$$\Phi_{\text{env},\alpha} \approx X_{\lambda\alpha} = \sum_{i=1}^{N-1} V_{\alpha\beta_i} S_{\lambda\beta_i}. \quad (13)$$

Thus, for any coordinates  $\beta_i$  in  $\beta$ , where  $\alpha \neq \beta_i$ , TeX decomposes the infrared signal  $S_{\lambda\alpha}$  at pixel coordinates  $\alpha = (x, y)$  as

$$S_{\lambda\alpha} = e_{\lambda\alpha} B_\lambda(T_\alpha) + (1 - e_{\lambda\alpha}) X_{\lambda\alpha}, \quad (14)$$

where  $V_{\alpha\beta_i}$  represents the linear combination vector between pixel  $\beta_i$  and pixel  $\alpha$ . The direction of thermal radiation is from pixel  $\beta_i$  towards pixel  $\alpha$ . However, predicting  $V_{\alpha\beta_i}$  between every pair of pixels has a complexity of  $\mathcal{O}(N^2)$ , which is computationally expensive.

To reduce complexity, TeX suggests dividing an infrared image into  $m$  grids and averaging, resulting in an  $m$ -dimensional vector. This division and local averaging equivalently downsample the full  $\mathbf{S}_\lambda \in \mathbf{R}^{H \times W}$  to  $\hat{\mathbf{S}}_\lambda \in \mathbf{R}^{m \times 1}$ . The components of  $\hat{\mathbf{S}}_\lambda$  are linearly combined to represent  $\Phi_{\text{env},\alpha}$ , with the corresponding linear coefficients  $\mathbf{V}_{\lambda\alpha} \in \mathbf{R}^{1 \times m}$ . The approximation of  $\Phi_{\text{env},\alpha}$  can be summarized as shown in Eq. (15), where  $\text{Ds}$  denotes average downsampling. This approach reduces the complexity to  $\mathcal{O}(N)$ .

$$\begin{aligned} X_{\lambda\alpha} &\approx \mathbf{V}_{\lambda\alpha} \hat{\mathbf{S}}_\lambda. \\ \hat{\mathbf{S}}_\lambda &= \text{Ds}(\mathbf{S}_\lambda). \end{aligned} \quad (15)$$

### 3.3. Superimposed infrared spectral image

According to [13], the TeX method necessitates additional filters in infrared cameras to capture infrared signals at different wavelengths. However, most currently available public datasets consist of infrared images captured directly by cameras without these filters, resulting in superimposed spectra infrared images. This discrepancy creates a gap between the TeX method and the general infrared images found in these datasets, making TeX unsuitable for infrared generative model.

To address this gap, we propose the TeV decomposition method. TeV overcomes the limitations of TeX by leveraging the material-specific emissivity assumption, which assumes a constant emissivity for a specific material. This allows TeV to handle the general images directly captured by infrared cameras without the need for multiple filters.

Our proposed TeV method eliminates the need for additional filters, making it more practical for real-world applications. Additionally, the TeV method is well-suited for the

physical constraints in infrared diffusion models. In the follow, we will introduce our TeV decomposition method in detail.

Based on Eq. (14) and Eq. (15), we propose Eq. (16), which represents the superimposition of multiple infrared spectral signals.  $[\lambda_{min}, \lambda_{max}]$  is the working wavelength range for infrared camera.

$$\int_{\lambda_{min}}^{\lambda_{max}} S_{\lambda\alpha} d\lambda = \int_{\lambda_{min}}^{\lambda_{max}} e_{\lambda\alpha} B_{\lambda}(T_{\alpha}) d\lambda + \int_{\lambda_{min}}^{\lambda_{max}} (1 - e_{\lambda\alpha}) \mathbf{V}_{\lambda\alpha} \hat{\mathbf{S}}_{\lambda} d\lambda. \quad (16)$$

Available data in [13] indicates that, the emissivity  $e_{\lambda}$  of most objects remains relatively constant across the working wavelengths of infrared cameras. The emissivities of common materials are shown in Appendix B. Therefore, we assume a constant emissivity for a specific material.

$$\mathcal{S}_{\alpha} = e_{\alpha} \int_{\lambda_{min}}^{\lambda_{max}} B_{\lambda}(T_{\alpha}) d\lambda + (1 - e_{\alpha}) \int_{\lambda_{min}}^{\lambda_{max}} \mathbf{V}_{\lambda\alpha} \hat{\mathbf{S}}_{\lambda} d\lambda. \quad (17)$$

We define the first integration as  $\mathbf{T}_{\alpha}$ , which represents the radiation emitted by the object itself at pixel  $\alpha$ .

$$\mathbf{T}_{\alpha} = \int_{\lambda_{min}}^{\lambda_{max}} B_{\lambda}(T_{\alpha}) d\lambda. \quad (18)$$

The second integration can also be simplified as a product of two matrices, which represents the reflective of other objects' radiation.

$$\begin{aligned} \int_{\lambda_{min}}^{\lambda_{max}} \mathbf{V}_{\lambda\alpha} \hat{\mathbf{S}}_{\lambda} d\lambda &= \underbrace{\mu_{\alpha} \int_{\lambda_{min}}^{\lambda_{max}} \mathbf{V}_{\lambda\alpha} d\lambda}_{\mathbf{V}_{\alpha}} \underbrace{\int_{\lambda_{min}}^{\lambda_{max}} \hat{\mathbf{S}}_{\lambda} d\lambda}_{\hat{\mathbf{S}}} \\ &= \mathbf{V}_{\alpha} \hat{\mathbf{S}}. \end{aligned} \quad (19)$$

Here,  $\hat{\mathbf{S}}$  represents the average downsampling result of the complete infrared image  $\mathcal{S}$ , corresponding to the operation described in Eq. (15).

$$\int_{\lambda_{min}}^{\lambda_{max}} \hat{\mathbf{S}}_{\lambda} d\lambda = \int_{\lambda_{min}}^{\lambda_{max}} \text{Ds}(\mathbf{S}_{\lambda}) d\lambda = \text{Ds}\left(\int_{\lambda_{min}}^{\lambda_{max}} \mathbf{S}_{\lambda} d\lambda\right) = \text{Ds}(\mathcal{S}) = \hat{\mathbf{S}}. \quad (20)$$

Thus, we can rewrite the decomposition equation for the superimposition of multiple infrared spectral signals, named as the **TeV decomposition method**.

$$\mathcal{S} = \mathbf{e}\mathbf{T} + (\mathbf{1} - \mathbf{e}) \mathbf{V}\hat{\mathbf{S}}, \quad (21)$$

where  $\mathbf{e} = \{e_{\alpha} | \alpha = (x, y)\} \in \mathbf{R}^{H \times W}$  represents the emissivity matrix,  $\mathbf{T} = \{\mathbf{T}_{\alpha} | \alpha = (x, y)\} \in \mathbf{R}^{H \times W}$  represents the temperature matrix,  $\mathbf{V} = \{\mathbf{V}_{\alpha} | \alpha = (x, y)\} \in \mathbf{R}^{H \times W \times m}$  represents the thermal vector matrix,  $\hat{\mathbf{S}} \in \mathbf{R}^{m \times 1}$  represents the average downsampling result



of input infrared image.  $\mathcal{S}$  is the captured image by infrared camera, and can be regarded as superimposition of multiple infrared spectral signals.  $\mathbf{T}$  is the radiation from object itself.  $\mathbf{e}$  and  $\mathbf{V}$  are emissivity and thermal vector matrix respectively.  $\hat{\mathcal{S}}$  represents the average downsampling result of the input infrared image  $\mathcal{S}$ .

Based on the derived relationship, we can train a self-supervised decomposition network  $\mathcal{N}_{\text{TeV}}$  to predict  $\mathbf{e}$ ,  $\mathbf{T}$ , and each  $\mathbf{V}$  by optimizing  $\mathbb{E}_{\mathcal{S} \in p_{\text{data}}} \|\tilde{\mathcal{S}} - \mathcal{S}\|_2^2$

$$\tilde{\mathbf{e}}, \tilde{\mathbf{T}}, \tilde{\mathbf{V}} = \mathcal{N}_{\text{TeV}}(\mathcal{S}), \quad (22)$$

where  $\mathcal{S}$  is the ground truth and  $\tilde{\mathcal{S}}$  is the reconstructed infrared image. Rec represents the reconstruction method as described in Eq. (21).

$$\tilde{\mathcal{S}} = \text{Rec}(\tilde{\mathbf{e}}, \tilde{\mathbf{T}}, \tilde{\mathbf{V}}). \quad (23)$$

### 3.4. Physics-informed loss

The translated infrared images from many previous works often violate physical laws. Based on the proposed TeV decomposition method, we introduce two physics-informed losses to supervise the diffusion model training.

#### 3.4.1. Physical reconstruction loss $\mathcal{L}_{\text{Rec}}$

The first loss is the reconstruction loss of the translated image, termed  $\mathcal{L}_{\text{Rec}}$ . If the diffusion model can accurately estimate and sample from the distribution of the infrared domain, the  $\mathcal{L}_{\text{Rec}}$  of the translated image  $\hat{\mathbf{x}}_0$  will be minimal. Otherwise, the loss will be large.  $\mathcal{L}_{\text{Rec}}$  acts like a discriminator in GANs but operates continuously in the diffusion model.

$$\mathcal{L}_{\text{Rec}} = \|\text{Rec}(\mathcal{N}_{\text{TeV}}(\hat{\mathbf{x}}_0)) - \hat{\mathbf{x}}_0\|_2^2. \quad (24)$$

#### 3.4.2. Physical TeV space loss $\mathcal{L}_{\text{TeV}}$

The second loss measures the discrepancy in the TeV space between the translated image and the ground truth, termed  $\mathcal{L}_{\text{TeV}}$ . This loss ensures that the translated images are similar to the ground truth in a higher-dimensional and more physically meaningful space.  $\mathcal{L}_{\text{TeV}}$  highlights physically unreasonable aspects of the translated images from the TeV space perspective.

$$\mathcal{L}_{\text{TeV}} = \|\mathcal{N}_{\text{TeV}}(\hat{\mathbf{x}}_0) - \mathcal{N}_{\text{TeV}}(\mathbf{x}_0)\|_2^2. \quad (25)$$

### 3.5. PID architecture

Combining efficient physical losses with the latent diffusion model, we propose the PID architecture, as shown in Fig. 3. First, we encode the ground truth infrared image  $\mathbf{x}_0$  using a VAE encoder  $\mathcal{E}$  to obtain  $\mathbf{z}_0$ . The RGB image  $\mathbf{x}_{\text{RGB}}$  is also encoded by a conditional encoder  $c_\theta$  to obtain  $\mathbf{c}_{\text{RGB}}$ .

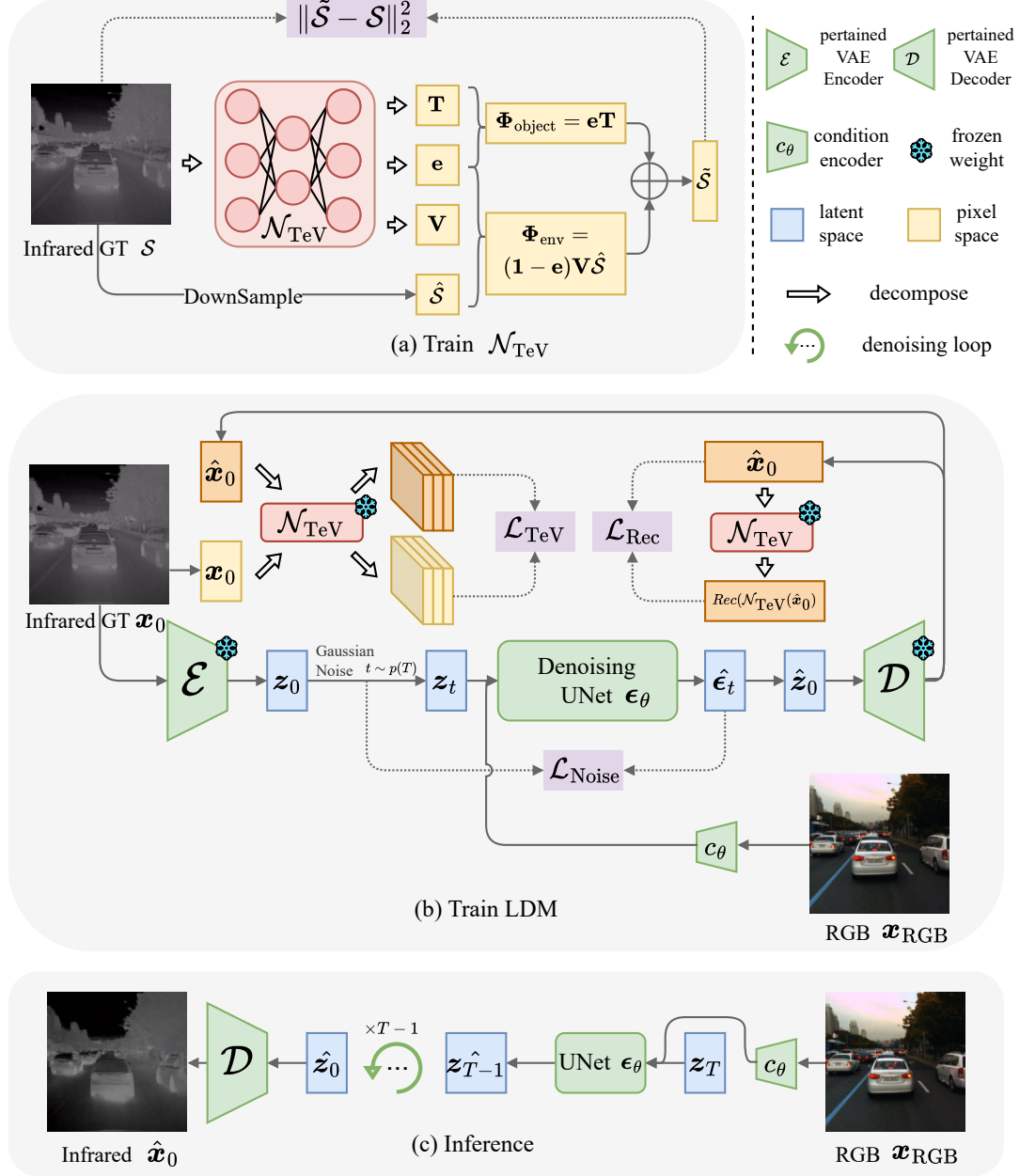


Fig. 3: The overview of our proposed PID. (a) Firstly, the PID trains a  $\mathcal{N}_{\text{TeV}}$  with self-supervised loss on infrared dataset. (b) Secondly, infrared GT images are encoded by the pretrained VQGAN encoder  $\mathcal{E}$  to obtain latent space vectors  $\mathbf{z}_0$ . Gaussian noise are then added to  $\mathbf{z}_0$  to produce intermediate vector  $\mathbf{z}_t$ . The denoising UNet is trained to predict the added noise, with the RGB image condition. In addition to  $\mathcal{L}_{\text{Noise}}$ ,  $\mathcal{L}_{\text{TeV}}$  and  $\mathcal{L}_{\text{Rec}}$  are also incorporated into the training process. During this process, the weights of VQGAN and  $\mathcal{N}_{\text{TeV}}$  are frozen, allowing PID to learn the infrared features and physical laws without increasing extra training parameters. (c) The inference process of PID.

$$\mathbf{z}_0 = \mathcal{E}(\mathbf{x}_0), \quad \mathbf{c}_{\text{RGB}} = c_\theta(\mathbf{x}_{\text{RGB}}). \quad (26)$$

Both  $\mathbf{z}_0$  and  $\mathbf{c}_{\text{RGB}}$  share the same latent spatial dimension  $H' \times W'$ . Then, Gaussian noise  $\epsilon$  is added to  $\mathbf{z}_0$  to obtain  $\mathbf{z}_t = \sqrt{\bar{\alpha}_t}\mathbf{z}_0 + \sqrt{1 - \bar{\alpha}_t}\epsilon$ .

We concatenate the conditional image  $\mathbf{c}_{\text{RGB}}$  with  $\mathbf{z}_t$  in the channel dimension. Then, a denoising model  $\epsilon_\theta(\mathbf{z}_t; t, \mathbf{c}_{\text{RGB}})$  is trained to predict the added noise  $\epsilon$ .

In addition to the loss between the predicted noise by the denoising UNet and the diffusion-added noise,  $\mathcal{L}_{\text{Noise}}(\epsilon, \epsilon_\theta)$ , we incorporate the proposed  $\mathcal{L}_{\text{Rec}}$  and  $\mathcal{L}_{\text{TeV}}$  produced by the frozen  $\mathcal{N}_{\text{TeV}}$  into the training of the denoising model.  $k_1$  and  $k_2$  are hyper-parameters.

Our PID method combines the iterative optimization capability of the diffusion model with the constraints of physical losses, resulting in images that better adhere to physical laws. The whole optimization goal is Eq. (27),

$$\begin{aligned} \theta_{PID}^* &= \arg \min_{\theta} \mathbb{E}_{\mathbf{x}_0 \sim p_{\text{data}}, \epsilon \sim \mathcal{N}(\mathbf{0}, \mathbf{I})} \\ &[\mathcal{L}_{\text{Noise}}(\epsilon, \epsilon_\theta(\mathbf{z}_t; t, \mathbf{c}_{\text{RGB}})) + k_1 \mathcal{L}_{\text{Rec}} + k_2 \mathcal{L}_{\text{TeV}}]. \end{aligned} \quad (27)$$

During inference, PID starts from  $t = T$  and samples Gaussian noise in the latent space. Then PID removes noise step by step until  $t = 0$ . Finally, the VAE decoder  $\mathcal{D}$  recovers the pixel space infrared image result  $\hat{\mathbf{x}}_0 = \mathcal{D}(\hat{\mathbf{z}}_0)$ . Specifically, the estimated  $\hat{\mathbf{x}}_0$  in the intermediate state  $\mathbf{z}_t$  can be written as

$$\hat{\mathbf{x}}_0 = \mathcal{D} \left( \frac{\mathbf{z}_t - \sqrt{1 - \bar{\alpha}_t}\epsilon_\theta}{\sqrt{\bar{\alpha}_t}} \right). \quad (28)$$

## 4. Experiments results and analysis

### 4.1. Implementation details

**Dataset:** According to Wien’s displacement law [34],

$$\lambda_{\text{max}} = \frac{b}{\text{Temperature}} = \frac{2898 \mu\text{m} \cdot \text{K}}{293.15 \text{K}} \approx 10 \mu\text{m}. \quad (29)$$

The wavelength of infrared images in real-world applications (20°C or 293.15K) with the strongest energy generally falls within the long-wavelength band. Therefore, **we select KAIST [14] (7.5–13.5  $\mu\text{m}$ ) and FLIR[35] (7.5–13.5  $\mu\text{m}$ ) datasets in our experiments, both of which lie within long-wavelength range.** We use 8347 image pairs for training and 1256 pairs for testing in FLIR. We use 12538 image pairs for training and 2252 image pairs for testing from the KAIST dataset.

**Training details:** All experiment images are cropped into centered squares according to their shortest side length. Subsequently, they are resized to  $512 \times 512$ . Both the training and validation sets undergo the same operations.

In the first stage,  $\mathcal{N}_{\text{TeV}}$  uses a UNet [36] with a ResNet18 [37] encoder. The number of channels for  $\mathbf{V}$  is set to  $m = 4$ . To ensure consistency between decomposition values and

their physical meanings, a sigmoid layer is used for the  $\mathbf{e}$  output layer, and a ReLU layer for the  $\mathbf{T}$  output layer. Two  $\mathcal{N}_{\text{TeV}}$  models are trained with self-supervision loss on the KAIST and FLIR training datasets until convergence, respectively.

In the second stage, the pretrained VQGAN-f8 [10] encodes the ground truth infrared images to  $64 \times 64 \times 4$  latent space vectors. The conditional visible RGB image is encoded to  $64 \times 64 \times 3$ . Self-attention layers are set in the spatial resolutions 8, 16, and 32 of UNet. During the training process, the weights of  $\mathcal{N}_{\text{TeV}}$  are frozen. The weights of the two losses are set to  $k_1 = 50, k_2 = 5$  on the KAIST dataset and  $k_1 = k_2 = 50$  on the FLIR dataset, respectively. We train for 60k iterations with a batch size of 48 for all diffusion models. A constant learning rate of 1e-6 is chosen for training. We set 1000 diffusion steps for training and 200 steps for inference using DDIM [26].

All baseline methods are adequately trained for the same number of iterations on the FLIR and KAIST datasets respectively for a fair comparison. Among them, EGGAN-O represents the official pretrained Edge-guided GAN provided by [4], while EGGAN-U and EGGAN-M stand for Edge-guided GAN based on UNIT [38] and MUNIT [39], respectively.

**Metrics:** We choose commonly used image similarity metrics, SSIM [15] and PSNR, as our metrics evaluation. Previous studies [11] indicate that LPIPS [40] and FID [41] may better reflect the perceptual quality of image generation, thus they have also been included in metrics evaluation.

Section 4.2 shows the performance of PID on the KAIST dataset and Section 4.3 shows the performance of our method on the FLIR dataset. Section 4.4 presents the ablation study of the proposed physical losses.

#### 4.2. Results on KAIST dataset

The KAIST dataset includes three typical scenes: campus, road, and downtown, each captured during both daytime and nighttime. These scenes feature essential elements for driving, such as roads, vehicles, and pedestrians.

Table 1: Quantitative results on the KAIST dataset. \* represents the available data on published papers. The best results are highlighted in **bold**, and the second-best results are underlined. The rows above and below the line represent GAN-based methods and LDM-based methods, respectively.

	SSIM $\uparrow$	PSNR $\uparrow$	LPIPS $\downarrow$	FID $\downarrow$
<b>Pix2Pix</b> [17]	0.69*	21.25*	0.196*	132.04
<b>CycleGAN</b> [18]	0.6016	17.02	0.2515	67.57
<b>ThermalGAN</b> [2]	0.66*	19.74*	0.242*	277.85
<b>InfraGAN</b> [3]	0.76*	22.97*	0.159*	222.96
<b>EGGAN-O</b> [4]	0.4486	9.91	0.3687	96.83
<b>EGGAN-U</b> [4, 38]	0.6260	17.07	0.2747	76.27
<b>EGGAN-M</b> [4, 39]	0.4782	10.65	0.3685	79.45
<b>LDM-vqf4</b> [10]	0.6025	14.77	0.1948	78.68
<b>LDM-vqf8</b> [10]	<u>0.7892</u>	<u>23.31</u>	<u>0.1380</u>	<u>64.54</u>
<b>PID-vqf8</b>	<b>0.7913</b>	<b>23.60</b>	<b>0.1366</b>	<b>51.69</b>

Table 1 shows the results on the KAIST dataset. We compare not only GAN-based methods but also LDM using different VQGANs. Specifically, vqf4 and vqf8 represent  $4\times$  and  $8\times$  VQGAN, respectively.

We introduce LDM into the field of infrared image translation, achieving significant improvements over GAN-based methods. The original LDM is enhanced by increasing the attention spatial resolution of the UNet to better suit infrared image translation. LDM-vqf8 surpasses the best GAN-based method, InfraGAN, by 0.0292 in SSIM, 0.34 in PSNR, a reduction of 0.021 in LPIPS, and a significant reduction of 158.42 in FID. It is observed that vqf8 performs better than vqf4 in this experiment, likely due to the limited compressed space of vqf4, which causes overfitting of the denoising UNet.

Our proposed PID method, which is based on LDM and incorporates physical losses, significantly surpasses the basic LDM method. It generates images that better align with the characteristics of the real infrared domain. Compared to LDM-vqf8, PID-vqf8 shows improvements of 0.0021 in SSIM, 0.29 in PSNR, a reduction of 0.0014 in LPIPS, and a significant reduction of 12.85 in FID. This quantitative evaluation supports the effectiveness of our proposed PID method, highlighting its superiority in enhancing the quality and realism of generated infrared images.

Fig. 4 shows the qualitative results on KAIST dataset. Our approach generates better high-level infrared semantic information than baseline methods. For instance, the road surface beneath cars shows strong signal intensity in the ground truth (Fig. 4a). PID and LDM accurately represent such details. PID emphasizes the physical properties of objects in images, resulting in clearer boundaries than LDM.

One of the main challenges of RGB-to-infrared translation is poor illumination in the RGB image input. Baseline methods perform suboptimally in these conditions. For example, in the EGGAN results shown in Fig. 4c, pedestrians, which are heat-emitting objects, appear cooler than the environment, violating physical laws. In contrast, PID focuses on the infrared physical properties of pedestrians, generating images with clear pedestrian shapes and demonstrating better robustness in translating nighttime images.

### 4.3. Results on FLIR dataset

The FLIR dataset contains scenes including urban roads and highways, among others, featuring elements such as roads, buildings, pedestrians, and vehicles. Data collection spans both well-lit daytime conditions and low-light nighttime conditions. Due to the lack of complete alignment between the two modalities in the original dataset, we conduct preprocessing to align the data.

We compare the performance on the FLIR dataset. Table 2 shows the quantitative results. LDM-based methods achieve better performance than GAN-based methods. For example, LDM-vqf8 obtains a PSNR of 17.13, an LPIPS of 0.3655, and an FID of 90.57, demonstrating its strong ability to generate high-quality infrared images. While InfraGAN achieves a slightly higher SSIM result of **0.4050**, it performs worse in other metrics, showing a trade-off between structural similarity and perceptual quality. InfraGAN has a PSNR of 16.95, LPIPS of 0.5050, and FID of 399.71, which are notably less effective compared to the performance of LDM-vqf8 and PID-vqf8.

Table 2: Quantitative metrics on FLIR dataset. The best results are highlighted in **bold**, and the second-best results are underlined. The rows above and below the line represent GAN-based methods and LDM-based methods, respectively.

	SSIM $\uparrow$	PSNR $\uparrow$	LPIPS $\downarrow$	FID $\downarrow$
Pix2Pix [17]	0.2986	16.34	0.3833	199.06
CycleGAN [18]	0.3451	12.74	0.4270	100.32
ThermalGAN [2]	0.1523	11.59	0.5981	407.01
InfraGAN [3]	<b>0.4050</b>	16.95	0.5050	399.71
EGGAN-O [4]	0.3464	9.65	0.5564	140.01
EGGAN-U [4, 38]	0.3745	14.30	0.4719	140.92
EGGAN-M [4, 39]	0.2904	10.32	0.4345	139.11
LDM-vqf4 [10]	0.3613	14.85	0.4035	108.98
LDM-vqf8 [10]	<u>0.4017</u>	<u>17.13</u>	<u>0.3655</u>	<u>90.57</u>
PID-vqf8	0.4006	<b>17.26</b>	<b>0.3599</b>	<b>84.26</b>

PID demonstrates exceptional performance, significantly outperforming baseline methods across multiple metrics. Compared to LDM-vqf8, PID-vqf8 shows an increase of 0.13 in PSNR, a decrease of 0.0056 in LPIPS, and a significant reduction of 5.89 in FID. When compared to InfraGAN, PID-vqf8 shows improvements of 0.31 in PSNR, a decrease of 0.1451 in LPIPS, and a significant reduction of 315.03 in FID.

By integrating physical losses, PID enhances its ability to generate images that accurately represent infrared characteristics. This enhancement enables PID to surpass the basic LDM method and significantly outperform GAN-based approaches, marking a substantial advancement in infrared image translation.

Fig. 5 represents the qualitative results on FLIR dataset. Cycle consistency-based methods like CycleGAN retain the characteristics of RGB images, and the translated results do not reflect the thermal information of objects present in infrared images (e.g., cars in Fig. 5a). Edge consistency-based methods focus on edge information and may produce results that do not align with the physical characteristics of objects. For example, in the Fig. 5b, the edges of a tree shadow in EGGAN methods are clear, but the infrared physical information of the shadow could be contrary to the actual situation. Our method considers both image semantic information and infrared physical laws, enabling the generation of infrared images that closely resemble real ones.

In Fig. 5, under low-light conditions at night, the quality of RGB images significantly deteriorates, placing higher demands on the model’s ability to extract semantic information. The images translated by GAN-based methods are either blurry or violate the physical laws of objects (e.g., cooler radiation from lights in EGGAN-O, in the Fig. 5c and Fig. 5d). The images translated by LDM are generally similar to the ground truth in overall effect but still show blurriness in details. Our proposed PID, promoting LDM, effectively generates nighttime infrared images with clear details (e.g., people and vehicles within red boxes in the Fig. 5c) and adheres to physical laws, demonstrating strong robustness.

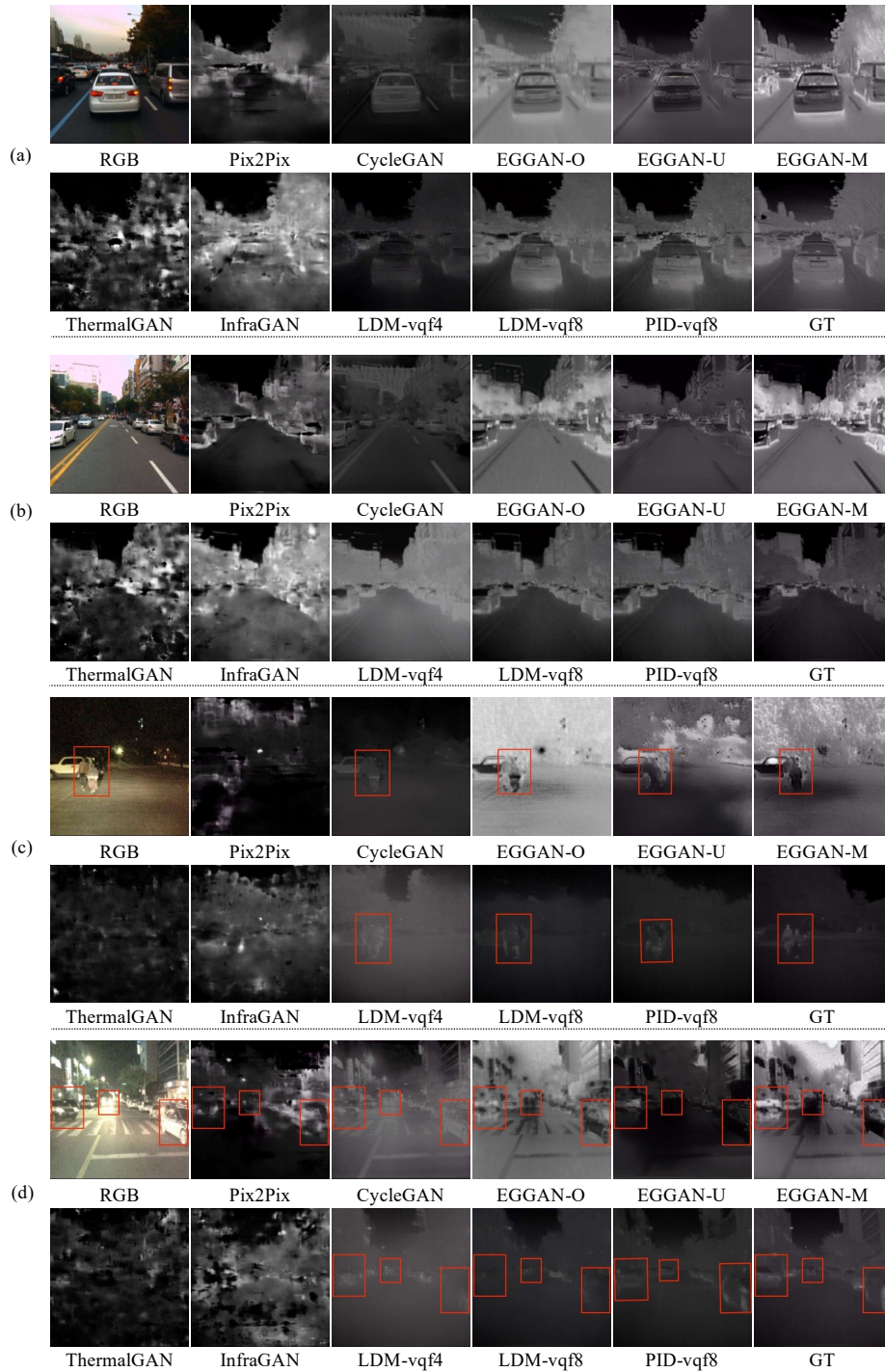


Fig. 4: Qualitative results on KAIST dataset. For the sake of clarity, the select objects in the images are highlighted with red boxes for easier comparison. PID demonstrates strong robustness in both daytime and nighttime scenes.

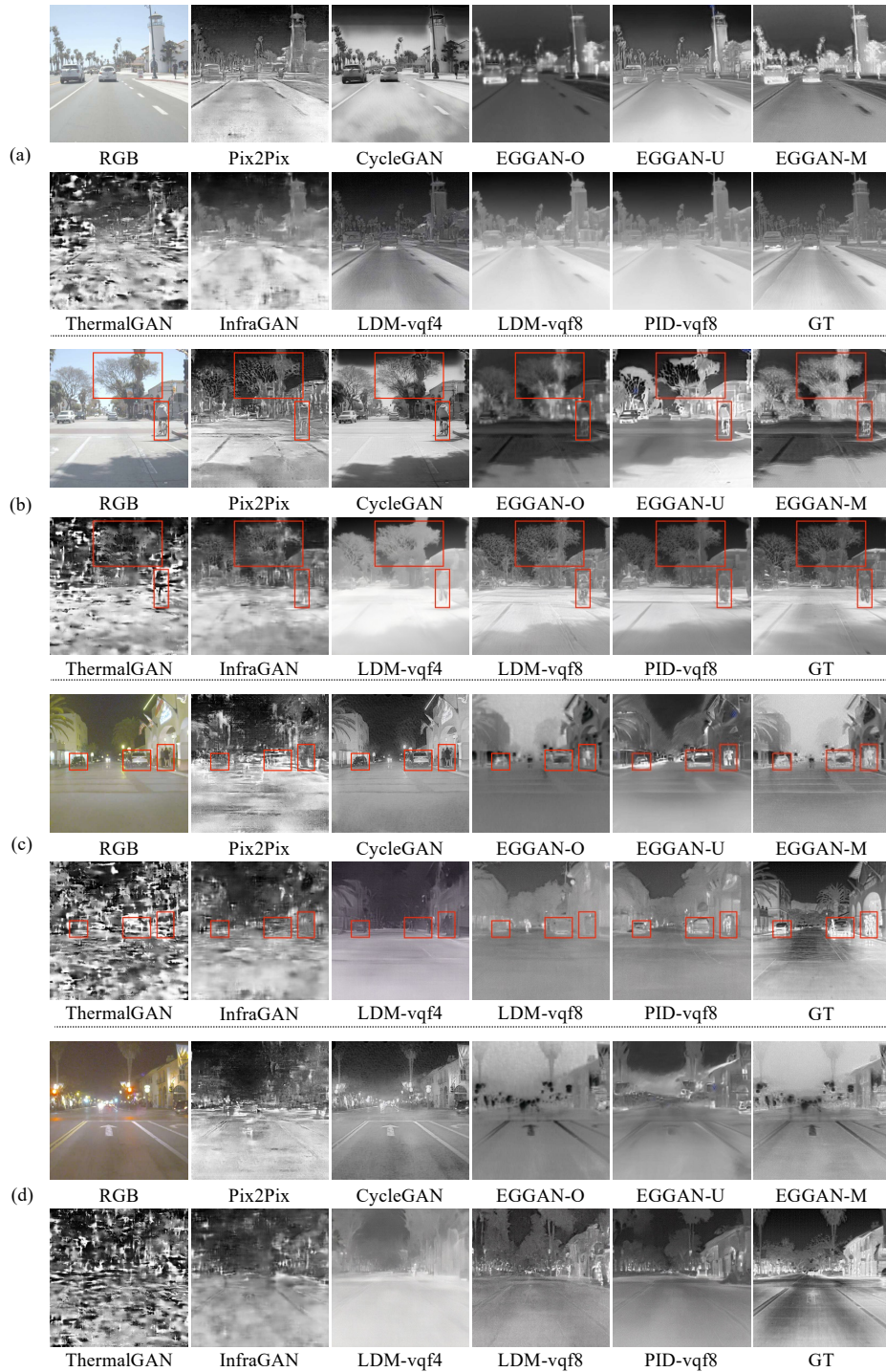


Fig. 5: Qualitative results on FLIR dataset. For the sake of clarity, the select objects in the images are highlighted with red boxes for easier comparison. Our PID provides detailed depictions of components such as people and trees in the scene, accurately representing the important thermal objects.



#### 4.4. Ablation study

##### 4.4.1. $\mathcal{N}_{\text{TeV}}$ architecture

Table 3: Training and testing  $\|\tilde{\mathcal{S}} - \mathcal{S}\|_2^2$  with different architectures of  $\mathcal{N}_{\text{TeV}}$ . Res50 means encoder of the net is resnet-50, res18 means resnet-18.  $m$  represents the channels of  $\mathbf{V}$  in Eq. (15).

Model	Param.	GFLOPS	$\mathcal{L}_{\text{Train}}$	$\mathcal{L}_{\text{Val}}$
PAN-res50, $m = 4$	24.26	34.95	2.59e-5	3.03e-5
UNet-res18, $m = 2$	14.33	21.82	8.70e-7	1.99e-6
UNet-res18, $m = 4$	14.33	21.90	2.11e-6	2.12e-6
UNet-res18, $m = 8$	14.33	22.05	1.77e-6	1.16e-6

To determine a suitable framework for  $\mathcal{N}_{\text{TeV}}$ , we test the reconstruction loss  $\|\tilde{\mathcal{S}} - \mathcal{S}\|_2^2$  of different frameworks. Both PAN (as used in [13]) and UNet are chosen for experiments. The dataset is KAIST dataset. All networks are trained 0.95k epochs.

As shown in Table 3, the UNet architecture generally demonstrates a lower reconstruction loss compared to PAN, indicating its superior capability in decomposing and reconstructing infrared images. Additionally, the UNet architecture is more lightweight, requires fewer parameters, and runs faster. Therefore, we chose UNet with a ResNet-18 encoder as the architecture for  $\mathcal{N}_{\text{TeV}}$ .

##### 4.4.2. The effectiveness of $\mathcal{L}_{\text{Rec}}$ and $\mathcal{L}_{\text{TeV}}$

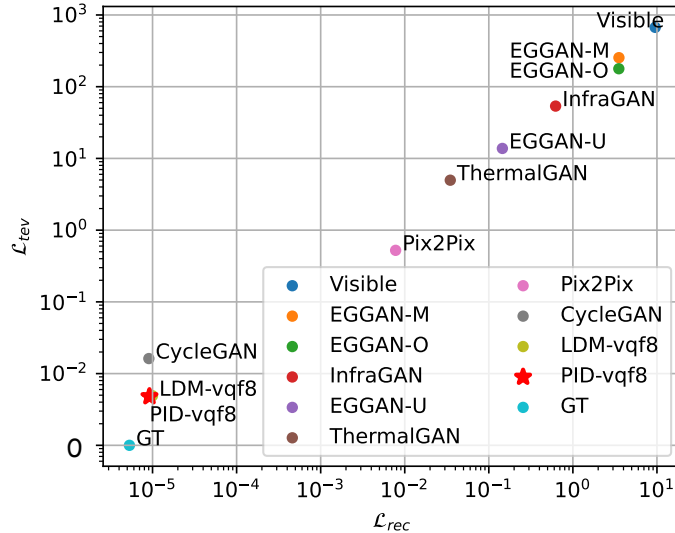


Fig. 6:  $\mathcal{L}_{\text{Rec}}$  and  $\mathcal{L}_{\text{TeV}}$  of different input images. Visible refers to visible RGB input, representing a high loss. Notably, PID shows remarkable results.

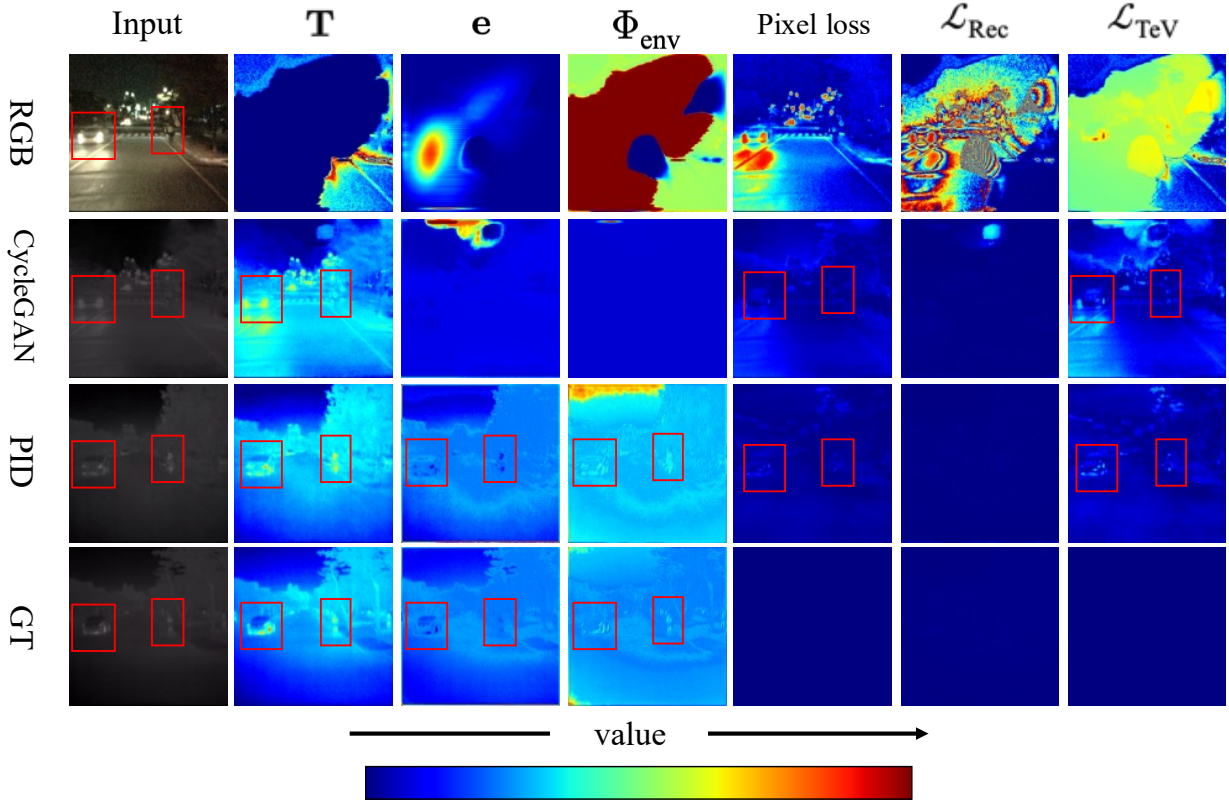


Fig. 7: Visualization of  $T$ ,  $e$ , and  $\Phi_{\text{env}}$ , as well as pixel loss and proposed physical losses. In PID and GT, the images show a clear distinction of pedestrians compared to the environment. Although the image translated by CycleGAN visually resembles the infrared image, it differs significantly from the GT in the TeV space. The proposed  $\mathcal{L}_{\text{Rec}}$  and  $\mathcal{L}_{\text{TeV}}$  provide a more accurate physical specificity than pixel loss.

$\mathcal{L}_{\text{Rec}}$  reflects the similarity between translated infrared images and real infrared domain images.  $\mathcal{L}_{\text{TeV}}$  represents the similarity between translated images based on input RGB images and the corresponding infrared images ground truth.

Fig. 6 shows  $\mathcal{L}_{\text{Rec}}$  and  $\mathcal{L}_{\text{TeV}}$  across translated images produced by different generative methods and GT images from the KAIST dataset. RGB images show the highest loss in both  $\mathcal{L}_{\text{Rec}}$  and  $\mathcal{L}_{\text{TeV}}$ , indicating the poorest performance in fitting the infrared domain. LDM and PID show significantly lower losses compared to baseline methods. This demonstrates that **LDM and PID have a stronger ability to fit the infrared domain.**

Fig. 7 shows the visualization of TeV decomposition quantities. The main objects in the chosen image are cars and a cyclist. This scene is influenced by glare and poor light conditions at night. CycleGAN does not predict the thermal radiation of the car and cyclist but retains the characteristics of RGB images. **PID provides clear descriptions of temperature  $T$ , emissivity  $e$ , and  $\Phi_{\text{env}}$  of objects in translated infrared images, thus our generated infrared images closer to the infrared image domain and GT reference.**

Fig. 7 also shows the visualization of proposed losses. RGB images and CycleGAN achieve higher losses than PID. This not only indicates the great generative ability of PID but also shows the infrared physical specificity of proposed losses.  $\mathcal{L}_{\text{Rec}}$  offers a continuous discriminator from other image domains toward the infrared image domain.  $\mathcal{L}_{\text{TeV}}$  better highlights pixels that deviate from expected infrared physical characteristics, such as thermal radiation from tires and pedestrians. In general, our proposed losses are explicitly effective and highly targeted toward the infrared target domain. With these losses, PID has a better generative ability to generate infrared images that adhere to physical laws.

#### 4.4.3. Loss proportion

Table 4: Ablation study on the loss proportion in PID. The best results are highlighted in **bold**, and the second-best results are underlined.

Dataset	$\mathcal{L}_{\text{rec}}$	$\mathcal{L}_{\text{TeV}}$	SSIM $\uparrow$	PSNR $\uparrow$	LPIPS $\downarrow$	FID $\downarrow$
KAIST	$k_1 = 0$	$k_2 = 0$	0.7892	23.31	0.1380	64.54
	$k_1 = 0$	$k_2 = 50$	0.7892	23.53	<u>0.1366</u>	50.99
	$k_1 = 50$	$k_2 = 0$	<u>0.7901</u>	<b>23.63</b>	<b>0.1363</b>	<b>50.17</b>
	$k_1 = 50$	$k_2 = 50$	0.7893	23.43	0.1370	<u>50.66</u>
	$k_1 = 50$	$k_2 = 5$	<b>0.7913</b>	<u>23.60</u>	<u>0.1366</u>	51.69
FLIR	$k_1 = 50$	$k_2 = 50$	<b>0.4006</b>	<u>17.26</u>	<u>0.3599</u>	<b>84.26</b>
	$k_1 = 50$	$k_2 = 5$	<u>0.3991</u>	<b>17.35</b>	<b>0.3577</b>	<u>84.28</u>

In this section, we conduct an ablation study on the proportion of  $\mathcal{L}_{\text{Rec}}$  and  $\mathcal{L}_{\text{TeV}}$ . We test five different proportions:  $\{k_1, k_2 | k_1 \in \{0, 50\}, k_2 \in \{0, 50\}\}$  and  $\{k_1 = 50, k_2 = 5\}$ . Table 4 shows the translated image quality evaluation. PID with only  $\mathcal{L}_{\text{Rec}}$  or  $\mathcal{L}_{\text{TeV}}$  (second and third rows) outperforms the baseline LDM. This proves the effectiveness of our proposed losses. As shown in Table 4,  $k_1 = 50, k_2 = 5$  in the fourth row has better performance than  $k_1 = 50, k_2 = 50$  in the third row. We observe that a slightly lower proportion of  $\mathcal{L}_{\text{TeV}}$  is beneficial for the model’s learning. We attribute this phenomenon to model overfitting. Translating infrared images based on RGB images is an underdetermined problem. Heavy matching dependency of  $\mathcal{L}_{\text{TeV}}$  may lead to overfitting. The model overly focuses on the distribution of the training dataset and ignores other potentially reasonable distributions.

#### 4.4.4. Dimensions of $\mathbf{V}$

Table 5: Ablation study on the hyperparameter  $m$  in Eq. (15). The best results are highlighted in **bold**, and the second-best results are underlined.

$\mathbf{V}$	SSIM $\uparrow$	PSNR $\uparrow$	LPIPS $\downarrow$	FID $\downarrow$
$m = 2$	0.7861	23.33	<u>0.1371</u>	<u>51.26</u>
$m = 4$	<b>0.7893</b>	<u>23.43</u>	<b>0.1370</b>	<b>50.66</b>
$m = 8$	<u>0.7885</u>	<b>23.51</b>	0.1392	51.73

In this section, we conduct an ablation study on the hyperparameter  $m$ , which represents the number of channels used to estimate  $\Phi_{\text{env}}$  in Eq. (15). We train  $\mathcal{N}_{\text{TeV}}$  with  $m \in \{2, 4, 8\}$ ,

embedding each into the PID framework. All experiments are conducted using the KAIST dataset with the loss proportions set as  $k_1 = k_2 = 50$ .

Table 5 presents the translated infrared image results. We observe that excessively high or low values of  $m$  are unsuitable for PID training. When  $m = 2$ , the lower number of decomposition channels in  $\mathbf{V}$  results in degraded estimations of  $\Phi_{\text{env}}$ , leading to poorer generative results. Conversely, with  $m = 8$ , the increased channels may cause overfitting of  $\mathcal{N}_{\text{TeV}}$ , impacting the overall PID training. When it comes to  $m = 4$ , the average downsampling grids precisely correspond to the four quadrants of an image. In Table 5,  $m = 4$  shows generally better evaluation results. Therefore, we choose  $m = 4$  for PID.

## 5. Conclusion

In this paper, we propose PID, combining latent diffusion model with infrared-specific physical losses for RGB-to-infrared image translation. PID excels in generating high-quality infrared images that adhere to infrared physical laws, outperforming existing methods. By leveraging the TeV decomposition method, we eliminate the need for camera filters and facilitate dataset utilization. The proposed  $\mathcal{L}_{\text{Rec}}$  and  $\mathcal{L}_{\text{TeV}}$  compensates for the generative model’s shortcomings in learning physical laws, enhancing the model’s interpretability. PID can be used to advance infrared image data augmentation with low cost. Future work will focus on improving  $\mathcal{N}_{\text{TeV}}$  accuracy and enhancing the diffusion model’s generative capacity, aiming for more realistic infrared image synthesis.

## Appendix A. Diffusion model derivation

The posterior distribution of the image after adding noise at different process steps can be written as the product of the posterior distributions:

$$q(\mathbf{x}_{1:T}|\mathbf{x}_0) = \prod_{t=1}^T q(\mathbf{x}_t|\mathbf{x}_{t-1}). \quad (\text{A.1})$$

In the diffusion model, the noise diffusion process is considered as a Markov chain[9]. The conditional probability distribution of the image after noise diffusion and the image in the previous process step is assumed to follow a Gaussian distribution, independent of earlier image distributions. The variance of noise in each iteration is represented by the scalar hyper-parameter  $\alpha_{1:T}$ , subjected to  $0 < \alpha_t < 1$ .

$$\begin{aligned} q(\mathbf{x}_t|\mathbf{x}_{t-1}) &= \mathcal{N}(\mathbf{x}_t|\sqrt{\alpha_t}\mathbf{x}_{t-1}, (1 - \alpha_t)\mathbf{I}). \\ \mathbf{x}_t &= \sqrt{\alpha_t}\mathbf{x}_{t-1} + \sqrt{1 - \alpha_t}\boldsymbol{\epsilon}, \\ \boldsymbol{\epsilon} &\sim \mathcal{N}(\mathbf{0}, \mathbf{I}). \end{aligned} \quad (\text{A.2})$$

The conditional probability distribution between different process step can be uniformly represented using the initial noise-free image  $\mathbf{x}_0$  and the parameter  $\bar{\alpha}_t$  corresponding to each

stage.

$$\begin{aligned}
\mathbf{x}_t &= \sqrt{\alpha_t} \mathbf{x}_{t-1} + \sqrt{1 - \alpha_t} \boldsymbol{\epsilon} \\
&= \sqrt{\alpha_t} \left( \sqrt{\alpha_{t-1}} \mathbf{x}_{t-2} + \sqrt{1 - \alpha_{t-1}} \boldsymbol{\epsilon} \right) + \sqrt{1 - \alpha_t} \boldsymbol{\epsilon} \\
&= \sqrt{\alpha_t \alpha_{t-1}} \mathbf{x}_{t-2} + \sqrt{1 - \alpha_t \alpha_{t-1}} \boldsymbol{\epsilon} \\
&= \sqrt{\alpha_t \alpha_{t-1} \dots \alpha_1} \mathbf{x}_0 + \sqrt{1 - \alpha_t \alpha_{t-1} \dots \alpha_1} \boldsymbol{\epsilon}.
\end{aligned} \tag{A.3}$$

This conditional probability distribution is also Gaussian distribution:

$$\begin{aligned}
q(\mathbf{x}_t | \mathbf{x}_0) &= \mathcal{N}(\mathbf{x}_t | \sqrt{\bar{\alpha}_t} \mathbf{x}_0, (1 - \bar{\alpha}_t) \mathbf{I}), \\
\bar{\alpha}_t &= \prod_{i=1}^t \alpha_i.
\end{aligned} \tag{A.4}$$

Given the image distribution of  $\mathbf{x}_0$  and  $\mathbf{x}_t$ , the posterior distribution of  $\mathbf{x}_{t-1}$  can be derived with some algebraic manipulation.

$$q(\mathbf{x}_{t-1} | \mathbf{x}_0, \mathbf{x}_t) = \mathcal{N}(\mathbf{x}_{t-1} | \boldsymbol{\mu}, \sigma^2 \mathbf{I}). \tag{A.5a}$$

$$\boldsymbol{\mu} = \frac{\sqrt{\bar{\alpha}_{t-1}} (1 - \alpha_t)}{1 - \bar{\alpha}_t} \mathbf{x}_0 + \frac{\sqrt{\alpha_t} (1 - \bar{\alpha}_{t-1})}{1 - \bar{\alpha}_t} \mathbf{x}_t. \tag{A.5b}$$

$$\sigma^2 = \frac{(1 - \bar{\alpha}_{t-1})(1 - \alpha_t)}{1 - \bar{\alpha}_t}. \tag{A.5c}$$

The q-process, which represents the noise diffusion process, is easily understood in the above equation. However, in the actual inference process (from  $\mathbf{x}_T$  to  $\mathbf{x}_0$ ), Eq. (A.5) requires prior knowledge of the image distribution  $\mathbf{x}_0$  at  $t = 0$  (i.e., the desired high-quality image), which contradicts the purpose of image generation. Therefore, additional work is required to optimize the denoising process

Given  $t$ , the noise-diffused image and the image at  $t = 0$  can be described based on Eq. (A.6).

$$\mathbf{x}_t = \sqrt{\bar{\alpha}_t} \mathbf{x}_0 + \sqrt{1 - \bar{\alpha}_t} \boldsymbol{\epsilon}, \boldsymbol{\epsilon} \sim \mathcal{N}(\mathbf{0}, \mathbf{I}). \tag{A.6}$$

Therefore, a denoising model  $\boldsymbol{\epsilon}_\theta$  can be trained to fit the noise at different diffusion process step.

$$\mathbb{E}_{(\mathbf{x} \sim p_{data})} \mathbb{E}_{\boldsymbol{\epsilon} \sim \mathcal{N}(\mathbf{0}, \mathbf{I})} \|\boldsymbol{\epsilon}_\theta(\mathbf{x}_t; t, \mathbf{c}) - \boldsymbol{\epsilon}\|_p^p. \tag{A.7}$$

The denoising process can be written as Eq. (A.8).

$$p_\theta(\mathbf{x}_{0:T} | \mathbf{x}) = p(\mathbf{x}_T) \prod_{t=1}^T p_\theta(\mathbf{x}_{t-1} | \mathbf{x}_t, \mathbf{c}), \tag{A.8a}$$

$$p(\mathbf{x}_T) = \mathcal{N}(\mathbf{x}_T | \mathbf{0}, \mathbf{I}), \tag{A.8b}$$

$$p_\theta(\mathbf{x}_{t-1} | \mathbf{x}_t, \mathbf{c}) = \mathcal{N}(\boldsymbol{\mu}_\theta(\mathbf{x}_t; t, \mathbf{c}), \sigma_t^2 \mathbf{I}). \tag{A.8c}$$

By revisiting the definition of  $\tilde{\mathbf{x}}$ , the denoising model can estimate the noise and obtain the distribution of the image at  $t = 0$ , denoted as  $\hat{\mathbf{x}}_0$ , thus avoiding the need for prior knowledge of the image distribution at  $t = 0$ .

$$\hat{\mathbf{x}}_0 = \frac{1}{\sqrt{\bar{\alpha}_t}} (\mathbf{x}_t - \sqrt{1 - \bar{\alpha}_t} \boldsymbol{\epsilon}_\theta(\mathbf{x}_t; t, \mathbf{c})). \tag{A.9}$$

By substituting the estimated  $\hat{\mathbf{x}}_0$  into Eq. (A.5)b, the mean  $\mu_\theta$  representing the p-process can be obtained. In this case, the variance  $\sigma^2$  of the normal distribution remains unchanged.

$$\boldsymbol{\mu}_\theta(\mathbf{x}_t; t, \mathbf{c}) = \frac{1}{\sqrt{\alpha_t}} \left( \mathbf{x}_t - \frac{1 - \alpha_t}{\sqrt{1 - \bar{\alpha}_t}} \boldsymbol{\epsilon}_\theta(\mathbf{x}_t; t, \mathbf{c}) \right). \quad (\text{A.10})$$

Based on Eq. (A.5) and Eq. (A.10), the iteration of inverse denoising process can be written as Eq. (A.11).

$$\begin{aligned} \mathbf{x}_{t-1} \leftarrow & \frac{1}{\sqrt{\alpha_t}} \left( \mathbf{x}_t - \frac{1 - \alpha_t}{\sqrt{1 - \bar{\alpha}_t}} \boldsymbol{\epsilon}_\theta(\mathbf{x}_t; t, \mathbf{c}) \right) \\ & + \sqrt{\frac{1 - \bar{\alpha}_{t-1}}{1 - \bar{\alpha}_t}} (1 - \alpha_t) \boldsymbol{\epsilon}, \boldsymbol{\epsilon} \sim \mathcal{N}(\mathbf{0}, \mathbf{I}). \end{aligned} \quad (\text{A.11})$$

The iterative denoising process starts with  $\mathbf{x}_T \sim \mathcal{N}(\mathbf{0}, \mathbf{I})$  and repeats the iterations according to Eq. (A.11) until  $t = 0$  to obtain a high-quality generation result  $\mathbf{x}_0$ .

## Appendix B. Emissivity of common materials

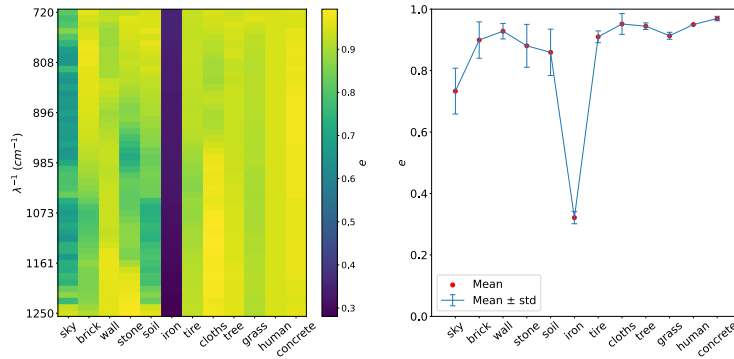


Fig. B.8: Common materials and their emissivities at different wavelengths.  $e$  represents emissivity,  $\lambda$  represents wavelength. TeX [13] collects the emissivities of some of the common materials in the figure. Left: the emissivities of different materials at different wavelengths. Right: the statistical result of the emissivities of different materials. Both figures indicate that emissivity of a special materials changes little at different wavelengths.

Fig. B.8 shows the emissivities of common materials as it varies with wavelength, with data sourced from [13]. According to the statistical results, we observe that the emissivities of most materials changes little with wavelength. Therefore, it can be approximately considered that specific materials have a constant emissivity.

## Acknowledgements

This work was supported in part by the National Natural Science Foundation of China under Grant No. U23B2034, No. 62203424, and No. 62176250, and in part by the Innovation Program of Institute of Computing Technology, Chinese Academy of Sciences under Grant No. 2024000112.

## References

- [1] C. Filippini, D. Perpetuini, D. Cardone, A. M. Chiarelli, A. Merla, Thermal infrared imaging-based affective computing and its application to facilitate human robot interaction: A review, *Applied Sciences* 10 (2020) 2924, <https://doi.org/10.3390/app10082924>.
- [2] V. V. Kniaz, V. A. Knyaz, J. Hladůvka, W. G. Kropatsch, V. Mizginov, Thermalgan: Multimodal color-to-thermal image translation for person re-identification in multispectral dataset, in: *ECCV Workshops*, 2018, [https://doi.org/10.1007/978-3-030-11024-6\\_46](https://doi.org/10.1007/978-3-030-11024-6_46).
- [3] M. A. Özkanoglu, S. Ozer, Infragan: A gan architecture to transfer visible images to infrared domain, *Pattern Recognit. Lett.* 155 (2022) 69–76, <https://doi.org/10.1016/j.patrec.2022.01.026>.
- [4] D.-G. Lee, M.-H. Jeon, Y. Cho, A. Kim, Edge-guided multi-domain rgb-to-tir image translation for training vision tasks with challenging labels, 2023 *IEEE International Conference on Robotics and Automation (ICRA)* (2023) 8291–8298, <https://doi.org/10.48550/arXiv.2301.12689>.
- [5] D. P. Kingma, M. Welling, Auto-encoding variational bayes, *arXiv abs/1312.6114*, <https://doi.org/10.48550/arXiv.1312.6114> (2013).
- [6] I. J. Goodfellow, J. Pouget-Abadie, M. Mirza, B. Xu, D. Warde-Farley, S. Ozair, A. C. Courville, Y. Bengio, Generative adversarial networks, *Communications of the ACM* 63 (2014) 139 – 144, <https://doi.org/10.48550/arXiv.1406.2661>.
- [7] G. Bredell, K. Flouris, K. Chaitanya, E. Erdil, E. Konukoglu, Explicitly minimizing the blur error of variational autoencoders, *ArXiv abs/2304.05939*, <https://doi.org/10.48550/arXiv.2304.05939> (2023).
- [8] B. Li, K. Xue, B. Liu, Y. Lai, Bbdm: Image-to-image translation with brownian bridge diffusion models, 2023 *IEEE/CVF Conference on Computer Vision and Pattern Recognition (CVPR)* (2022) 1952–1961, <https://doi.org/10.48550/arXiv.2205.07680>.
- [9] J. Ho, A. Jain, P. Abbeel, Denoising diffusion probabilistic models, *ArXiv abs/2006.11239*, <https://doi.org/10.48550/arXiv.2006.11239> (2020).
- [10] R. Rombach, A. Blattmann, D. Lorenz, P. Esser, B. Ommer, High-resolution image synthesis with latent diffusion models, 2022 *IEEE/CVF Conference on Computer Vision and Pattern Recognition (CVPR)* (2021) 10674–10685, <https://doi.org/10.48550/arXiv.2112.10752>.
- [11] C. Saharia, J. Ho, W. Chan, T. Salimans, D. J. Fleet, M. Norouzi, Image super-resolution via iterative refinement, *IEEE Transactions on Pattern Analysis and Machine Intelligence* 45 (2021) 4713–4726, <https://doi.org/10.1109/TPAMI.2022.3204461>.
- [12] A. Blattmann, R. Rombach, H. Ling, T. Dockhorn, S. W. Kim, S. Fidler, K. Kreis, Align your latents: High-resolution video synthesis with latent diffusion models, in: *Proceedings of the IEEE/CVF Conference on Computer Vision and Pattern Recognition*, 2023, pp. 22563–22575, <https://doi.org/10.48550/arXiv.2304.08818>.
- [13] F. Bao, X. Wang, S. H. Sureshbabu, G. Sreekumar, L. Yang, V. Aggarwal, V. N. Boddeti, Z. Jacob, Heat-assisted detection and ranging, *Nature* 619 (2023) 743–748, <https://doi.org/10.1038/s41586-023-06174-6>.
- [14] S. Hwang, J. Park, N. Kim, Y. Choi, I.-S. Kweon, Multispectral pedestrian detection: Benchmark dataset and baseline [dataset], 2015 *IEEE Conference on Computer Vision and Pattern Recognition (CVPR)* (2015) 1037–1045, <https://doi.org/10.1109/CVPR.2015.7298706>.
- [15] R. Guissin, E. Lavi, A. Palatnik, Y. Gronau, E. Repasi, W. Wittenstein, R. Gal, M. Ben-Ezra, Irisim: infrared imaging simulator, in: *SPIE Defense + Commercial Sensing*, 2005, <https://doi.org/10.1117/12.606524>.
- [16] M. Mirza, S. Osindero, Conditional generative adversarial nets, *ArXiv abs/1411.1784*, <https://doi.org/10.48550/arXiv.1411.1784> (2014).
- [17] P. Isola, J.-Y. Zhu, T. Zhou, A. A. Efros, Image-to-image translation with conditional adversarial networks, 2017 *IEEE Conference on Computer Vision and Pattern Recognition (CVPR)* (2016) 5967–5976, <https://doi.org/10.48550/arXiv.1611.07004>.
- [18] J.-Y. Zhu, T. Park, P. Isola, A. A. Efros, Unpaired image-to-image translation using cycle-consistent adversarial networks, 2017 *IEEE International Conference on Computer Vision (ICCV)* (2017) 2242–2251, <https://doi.org/10.1109/ICCV.2017.244>.

- [19] L. Zhang, A. Gonzalez-Garcia, J. van de Weijer, M. Danelljan, F. S. Khan, Synthetic data generation for end-to-end thermal infrared tracking, *IEEE Transactions on Image Processing* 28 (2018) 1837–1850, <https://doi.org/10.1109/TIP.2018.2879249>.
- [20] L. An, J. Zhao, H. Di, Generating infrared image from visible image using generative adversarial networks, 2019 IEEE International Conference on Unmanned Systems (ICUS) (2019) 157–161, <https://doi.org/10.1109/ICUS48101.2019.8995962>.
- [21] X. Qian, M. Zhang, F. Zhang, Sparse gans for thermal infrared image generation from optical image, *IEEE Access* 8 (2020) 180124–180132, <https://doi.org/10.1109/ACCESS.2020.3024576>.
- [22] C. Devaguptapu, N. Akolekar, M. Sharma, V. N. Balasubramanian, Borrow from anywhere: Pseudo multi-modal object detection in thermal imagery, 2019 IEEE/CVF Conference on Computer Vision and Pattern Recognition Workshops (CVPRW) (2019) 1029–1038, <https://doi.org/10.1109/CVPRW.2019.00135>.
- [23] S. Güzel, S. Yavuz, Infrared image generation from rgb images using cyclegan, in: 2022 International Conference on INnovations in Intelligent SysTems and Applications (INISTA), 2022, pp. 1–6, <https://doi.org/10.1109/INISTA55318.2022.9894231>.
- [24] X. Yi, H. Pan, H. Zhao, P. Liu, C. Zhang, J. Wang, H. Wang, Cycle generative adversarial network based on gradient normalization for infrared image generation, *Applied Sciences*, <https://doi.org/10.3390/app13010635> (2023).
- [25] Y. Song, J. N. Sohl-Dickstein, D. P. Kingma, A. Kumar, S. Ermon, B. Poole, Score-based generative modeling through stochastic differential equations, *ArXiv abs/2011.13456*, <https://doi.org/10.48550/arXiv.2011.13456> (2020).
- [26] J. Song, C. Meng, S. Ermon, Denoising diffusion implicit models, *ArXiv abs/2010.02502*, <https://doi.org/10.48550/arXiv.2010.02502> (2020).
- [27] D. P. Kingma, T. Salimans, B. Poole, J. Ho, Variational diffusion models, *ArXiv abs/2107.00630*, <https://doi.org/10.48550/arXiv.2107.00630> (2021).
- [28] A. Ramesh, P. Dhariwal, A. Nichol, C. Chu, M. Chen, Hierarchical text-conditional image generation with clip latents, *ArXiv abs/2204.06125*, <https://doi.org/10.48550/arXiv.2204.06125> (2022).
- [29] B. Kawar, M. Elad, S. Ermon, J. Song, Denoising diffusion restoration models, *ArXiv abs/2201.11793*, <https://doi.org/10.48550/arXiv.2201.11793> (2022).
- [30] A. R. Gillespie, S. Rokugawa, T. Matsunaga, J. S. Cothorn, S. J. Hook, A. B. Kahle, A temperature and emissivity separation algorithm for advanced spaceborne thermal emission and reflection radiometer (aster) images, *IEEE Trans. Geosci. Remote. Sens.* 36 (1998) 1113–1126, <https://doi.org/10.1117/12.255172>.
- [31] M. Planck, The theory of heat radiation, *Entropie* 144 (190) (1900) 164.
- [32] M. Kaviany, A. M. Kanury, Principles of heat transfer, 2001, <https://doi.org/10.1007/978-1-4899-0345-7.2>.
- [33] F. P. Incropera, D. P. Dewitt, T. L. Bergman, A. S. Lavine, Principles of heat and mass transfer, 2018.
- [34] D. J. Griffiths, Introduction to electrodynamics, 2017, <https://doi.org/10.1119/1.4766311>.
- [35] T. FLIR, Flir thermal dataset version 1.3 [dataset], <https://www.flir.com/oem/adas/adas-dataset-form/> (accessed 25 June 2024) (2019).
- [36] O. Ronneberger, P. Fischer, T. Brox, U-net: Convolutional networks for biomedical image segmentation, *ArXiv abs/1505.04597*, <https://doi.org/10.48550/arXiv.1505.04597> (2015).
- [37] K. He, X. Zhang, S. Ren, J. Sun, Deep residual learning for image recognition, 2016 IEEE Conference on Computer Vision and Pattern Recognition (CVPR) (2015) 770–778 <https://doi.org/10.48550/arXiv.1512.03385>.
- [38] M.-Y. Liu, T. M. Breuel, J. Kautz, Unsupervised image-to-image translation networks, in: *Neural Information Processing Systems*, 2017, <https://doi.org/10.48550/arXiv.1703.00848>.
- [39] X. Huang, M.-Y. Liu, S. J. Belongie, J. Kautz, Multimodal unsupervised image-to-image translation, in: *European Conference on Computer Vision*, 2018, [https://doi.org/10.1007/978-3-030-01219-9\\_11](https://doi.org/10.1007/978-3-030-01219-9_11).
- [40] R. Zhang, P. Isola, A. A. Efros, E. Shechtman, O. Wang, The unreasonable effectiveness of deep features as a perceptual metric, 2018 IEEE/CVF Conference on Computer Vision and Pattern Recognition



- (2018) 586–595, <https://doi.org/10.1109/CVPR.2018.00068>.
- [41] M. Heusel, H. Ramsauer, T. Unterthiner, B. Nessler, S. Hochreiter, Gans trained by a two time-scale update rule converge to a local nash equilibrium, in: *Neural Information Processing Systems*, 2017, <https://doi.org/10.48550/arXiv.1706.08500>.